Simulation of Polymer Melt Flow During Welding

A simulation approach to predict material and thermal properties during polymer welding as well as flash

BY M. MARCUS AND E. SANCAKTAR

Abstract

Polymer welding is used to join a wide variety of critical assemblies. These applications require careful melt control to prevent internal contamination, avoid external flash, and maximize the fill of polymer into the weld geometry for optimal strength. Currently, there are no commercially available modeling software packages to enable the simulation of polymer melt flow during welding. In this work, a commercially available injection molding software is adapted to simulate the welding process. The adaptation is helpful for predicting melt flow and potentially other important factors like intermolecular diffusion, chain orientation, and crystallinity.

Keywords

- Plastic Welding
- Modeling Plastic Welding
- Weld Melt Flow

Introduction

There is a variety of useful information about a polymer weld that could be determined via simulation. Some of this information includes intermolecular diffusion, polymer chain orientation, crystallinity, and the geometry of the weld flash. The flow of the melt in the weld area affects temperature, viscosity, orientation of polymer chains, and crystallinity. While all of these will impact the final strength of the weld, the temperature and polymer melt viscosity history change the efficiency of intermolecular diffusion, which may be the core contributor to weld strength for plastics.

The strength of polymers is always greater parallel to the polymer chain orientation rather than perpendicular, meaning that chain orientation is critical. The crystallinity of the material is also a fundamental component of overall strength. Lastly, the melt distribution affects the location and size of stress concentration points in the assembly geometry, significantly affecting fracture strength.

The viscosity of a polymer melt changes with shear stress (i.e., shear rate) and temperature (Refs. 1, 2). While viscosity generally decreases as temperature increases, the change in viscosity with shear (i.e., flow) is less consistent. For example, polymers can be shear thinning or thickening, meaning the viscosity may increase or decrease with increased shear rate.

If a simple flat joint were employed in a welded part, the flow could be modeled via equations of motion to find the shear stress in the melt, a method commonly used in research (Refs. 3, 4). However, modeling the melt flow is complex and challenging, even using a 1D model (Refs. 5, 6).

For a weld joint with no energy director, flow occurs at the contact points between surface asperities, the small irregularities caused by imperfect surface smoothness, as shown in Fig. 1.

As these asperities melt, the total surface contact area (i.e., the weld area) increases, which correlates to increased weld strength. One method to model this is the Lee and Springer method:

$$D_{ic}(x) = \frac{1}{w^*}\left[1 + a^* \int_0^t \frac{P_{app}}{\eta(T(x))}\right]^{1/5} \quad (1)$$

where D_{ic} is the degree of intimate contact, w* and a* are related to interfacial roughness, P_{app} is the static load, and $\eta(T(x))$ is viscosity as a function of temperature and distance (Ref. 7).

However, when flat-to-flat surfaces are welded via ultrasonics, there are several negative effects: increased power is required, control of flash location is reduced, and the marking of the parts is often increased. For this reason, most plastic welding applications use features that create intended small areas of contact between the two parts to be welded, which can come in the form of energy directors or sometimes shear joints.

https://doi.org/10.29391/2025.104.005

Due to this complex geometry, modeling of the melt flow is recommended using a computer-aided design (CAD) approach. While no software is available to model welding, several software packages have been designed to model melt flow for injection molding processes. In this work, MoldEx 3D was selected to be adapted to model melt flow during polymer welding.

This work demonstrates that melt flow simulation using currently available software typically used for injection molding can be applied to find reasonable predictions of temperature and viscosity history in the weld, shear rate, and extent of flow during the welding process. These outputs can then be applied to arithmetic equations for polymer chain orientation, diffusion, and stress concentration factors, which are useful for predicting the final weld quality.

Theory

Intermolecular Diffusion

Intermolecular diffusion is the movement of polymer chains across boundaries, from melt generated from one side of the joint to melt generated by the other side, or into any solid polymer surface with which melt comes into contact. The depth of these polymer chains moving into the boundary's other side can be termed interpenetration depth (Refs. 8, 9).

In 1949, Voyutski proposed the basic equation for interpenetration depth, X (Ref. 10):

$$X \propto e^{-E/2RT} t^{1/2} \tag{2}$$

where E is diffusion activation energy, R is molar gas constant, T is temperature, and t is time.

A common approach to thinking about intermolecular diffusion of polymer chains is in terms of reptation, which considers the polymer chain to be completely enclosed in a tube. Over time, the ends of the polymer chain will exit the tube, and then gradually, more of the chain diffuses until the entire chain has migrated from its original tube into a new tube. In this case, healing is considered the time for a polymer chain to diffuse entirely from its original tube into a new one. A weld is considered to retain full strength if fully healed (Refs. 11–14).

An isothermal healing model considering intermolecular diffusion by reptation has been proposed by Bastien and Gillespie (Ref. 15)

$$D_h(t) = \frac{\sigma}{\sigma_\infty} = \sum_{t=0}^{t/\Delta t} \left[\frac{{t_{i+1}}^{1/4} - {t_i}^{1/4}}{{t_R^*}^{1/4}} \right] \tag{3}$$

where $D_h(t)$ is the degree of healing as a function of time, σ/σ_∞ is the ratio of weld strength versus ideal weld strength (complete healing), and t_R is the reptation time for an entire polymer chain to diffuse out of its initial tube.

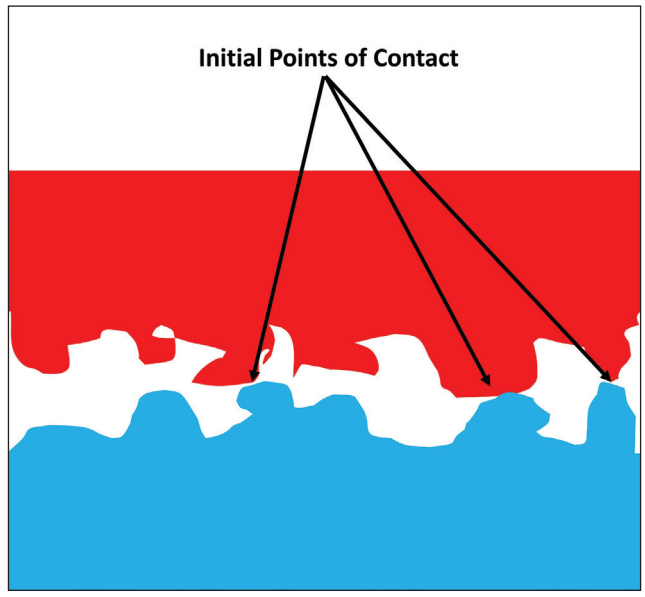

Fig. 1 — Diagram of how surface roughness leads to individual points of contact on a flat-to-flat joint surface.

However, any welding process is decidedly non-isothermal. This limitation led Yang and Pitchumani to develop a non-isothermal healing model of reptation (Ref. 16):

$$D_h(t) = \left[\int_0^t \frac{1}{t_w(T)} dt \right]^{1/4} \tag{4}$$

where $D_h(t)$ is the degree of healing as a function of time (1, when fully healed), and $t_w(T)$ is welding time, defined as the time for an entire polymer chain to diffuse out of its initial tube.

The relationship of healing to the ¼ power of time is referenced in other approaches to model the diffusion of polymer chains across a weld or knit line and has been experimentally verified (Refs. 17–19).

For example, Grewell and Benatar proposed the following equation for the degree of welding to jointly account for the effects of squeeze flow and intermolecular diffusion (Ref. 20):

$$DW(T,t)_h = \sum_{t=0}^{t=t'} \Gamma e^{\frac{-A_0 e^{[k_a T]}}{kT}} t^{1/4} \tag{5}$$

where T is temperature, t is time, Γ is the squeeze flow and heating coefficient, A_0 is a material constant, and k_a is the temperature parameter (1/k) that is the resultant of the activation energy divided by the Boltzmann constant (k), all parameters to be determined experimentally.

However, the Grewell-Benatar approach requires the measurement of material properties specific to that modeling approach, which limits the implementation of such a modeling method in the industry.

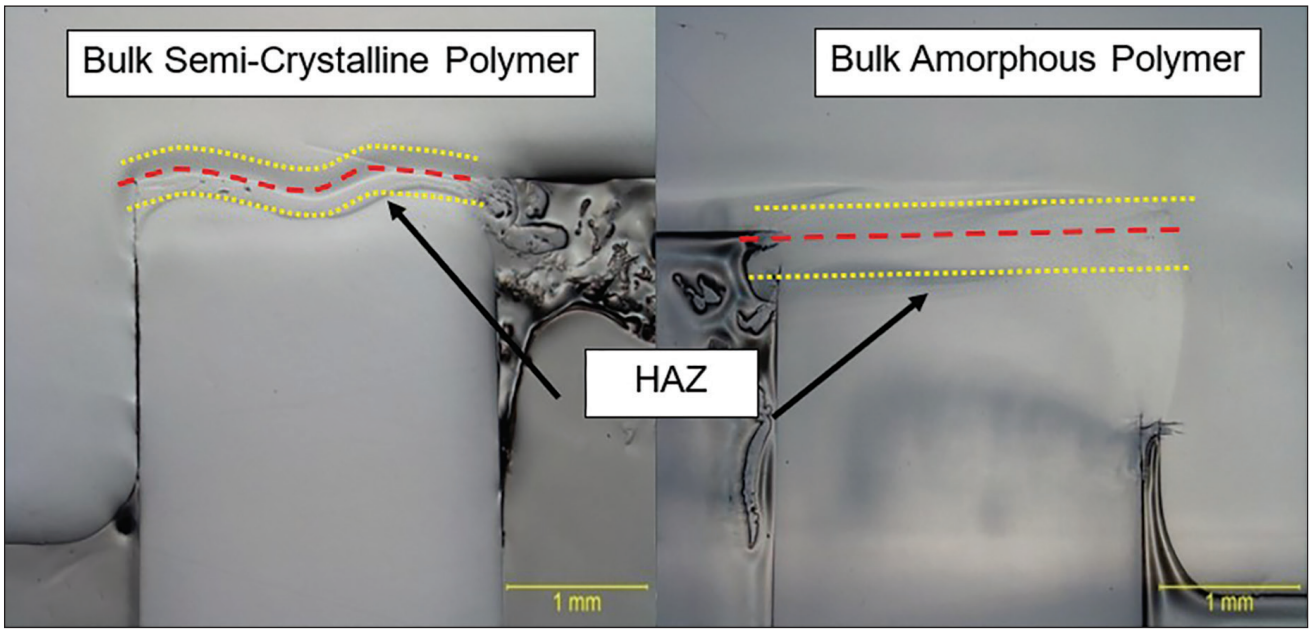

Fig. 2 — Sections of ultrasonically welded plastic parts showing differentiation between the HAZ and the bulk polymer (yellow dotted lines).

A reptation model can determine the welding time (i.e., in the Yang and Pitchumani equation). The most often used reptation models are the Doi-Edwards and the Rouse models. While the Rouse model was established first, the Doi-Edwards model is generally considered a better representative of intermolecular diffusion (Refs. 21–23). Bousmina established that the Rouse model is effective for interfaces where there is an excess of chain ends. Meanwhile, the Doi-Edwards model guided the behavior of melt interfaces where there are no excess chain ends. Most chain ends will not be at the surface during welding of injection-molded parts, so the Doi-Edwards model is more useful (Ref. 14).

Thus, the welding time, $t_w(T)$, can be approximated by the Doi-Edwards disentanglement time, or the time for a Gaussian chain to diffuse out of its tube, τ_d: (Ref. 24):

$$\tau_d = \frac{\zeta L^2}{\pi^2 K_B T} \quad (6)$$

where τ_d is diffusion time, ζ is the monomeric friction factor, L is the characteristic length of the polymer chain, K_B is the Boltzmann constant, and T is the temperature.

The monomeric friction factor depends on viscosity per (Refs. 25–27):

$$\zeta = \frac{36 M_0 \eta}{\rho N_A R^2} \quad (7)$$

where M_0 is the monomer molecular weight, η is the viscosity, ρ is the density, N_A is Avogadro's number, and R is the characteristic length of the polymer chain.

Chain Orientation

It has been noted that there is a distinct separation between the bulk material and material melted during welding when a welded polymer joint is sectioned and heat treated to allow the surface polymer chains to relax. Even in welds without separation, indicating good intermolecular diffusion, this distinction at the edge of the heat-affected zone (HAZ) is noted, as shown in Fig. 2 (Ref. 28).

In both cases, there is no line of separation through the middle of the weld where the two melt regions converged (indicated by the dashed red line in Fig. 2), but there is a line that divides the bulk polymer from the HAZ. This line indicates a change in the polymer structure from the bulk to the weld joint. It is proposed that this structural difference is due to differing factors for amorphous and semi-crystalline polymers. For the amorphous polymer, the HAZ has a change in orientation. For the semi-crystalline polymer, the HAZ has a change in crystallinity. Therefore, even in a weld that achieves complete fusion in terms of intermolecular diffusion across the joint, the weld strength will be weaker than the bulk due to this change in microstructure.

The orientation of polymer chains can significantly affect weld strength. This is only a primary influence for amorphous polymers. For semi-crystalline polymers, the chains will reorganize into spherulites as the polymer cools. For amorphous polymers, the highly oriented polymer chains induced by a high rate of shear flow will lead to anisotropy and a reduction in tensile strength (Ref. 29).

The effect on assembly strength of bond orientation has been especially noted and studied in fused deposition modeling (a type of 3D printing) using acrylonitrile butadiene styrene polymer (Refs. 30–32). Various levels of analysis have been applied to investigate the effect of raster angle, or the orientation of deposited layers to the tensile direction,

on strength. Transverse interfaces have been shown to provide 75-85% of the strength of parallel interfaces (Refs. 33, 34). Additionally, transverse interfaces result in more brittle failure (Refs. 35, 36). While these observations are related to the orientation of the bond interfaces, they may not directly relate to polymer chain orientation due to many additional factors present in 3D printing.

Observations similar to what is described above have been made for welded assemblies. A comparison of the microstructure of hot plate versus vibration welds, performed by Shieu, Wang, and Wu, demonstrated this. During hot plate welding, the shear flow-induced orientation of the polymer chains parallel to the weld joint results in a tensile strength of just 30% of the bulk. Conversely, vibration welding produced a more randomly oriented, isotropic orientation of the polymer chains, resulting in a tensile strength of 80% of the bulk (Ref. 37).

One way to predict the polymer chain orientation is based on the shape (Fig. 3) of the polymer chains and the shear rate applied to the melt, per Equation 8, where Brownian motion is negligible, and the Peclet number is much greater than one (Ref. 38):

$$\tan\phi = r\tan\left(\frac{\dot{\gamma}t}{r + 1/r}\right) \quad (8)$$

where Φ is the change in the orientation trajectory, r is a shape factor as defined in Fig. 3, $\dot{\gamma}$ is the shear rate, and t is the time underflow.

For most polymers, r is significantly greater than one. For a rod-like polymer, r can be estimated at ten. This approach considers the orientation vector along the "a" axis (Fig. 3). The Peclet number is the ratio of advective to diffusive flow. Essentially, the Peclet number is high if the motion of the molecules is dominated by bulk flow significantly more than diffusional flow, which would be true in the case of expelled polymer melt.

The most common method to measure chain orientation is a qualitative analysis of optical birefringence. Materials

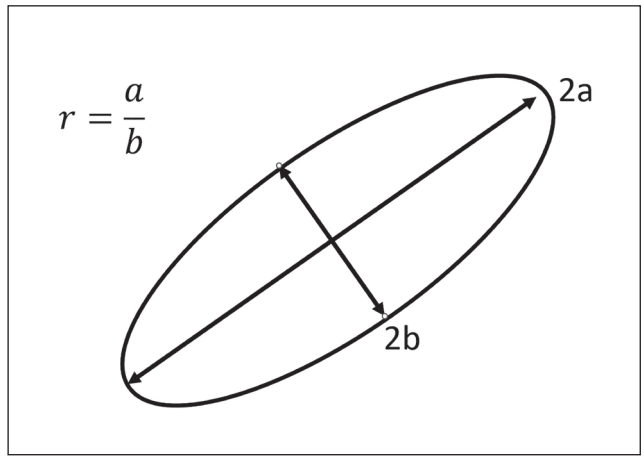

Fig. 3 — Geometry of polymer spheroid.

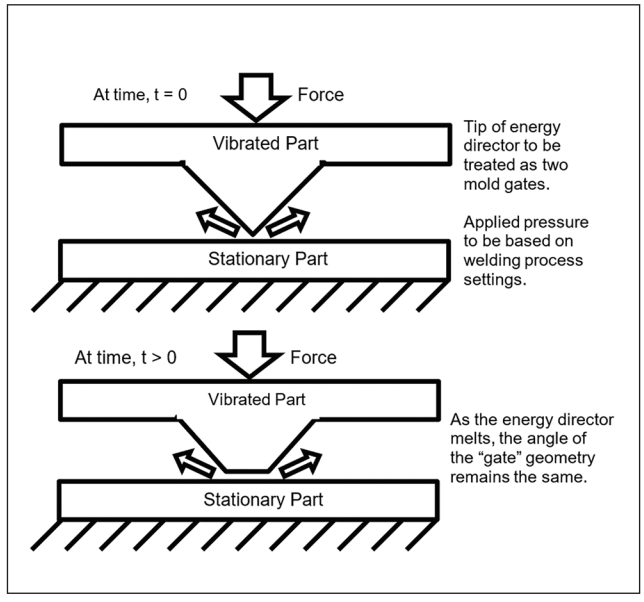

Fig. 4 — Diagram of approach to flow modeling.

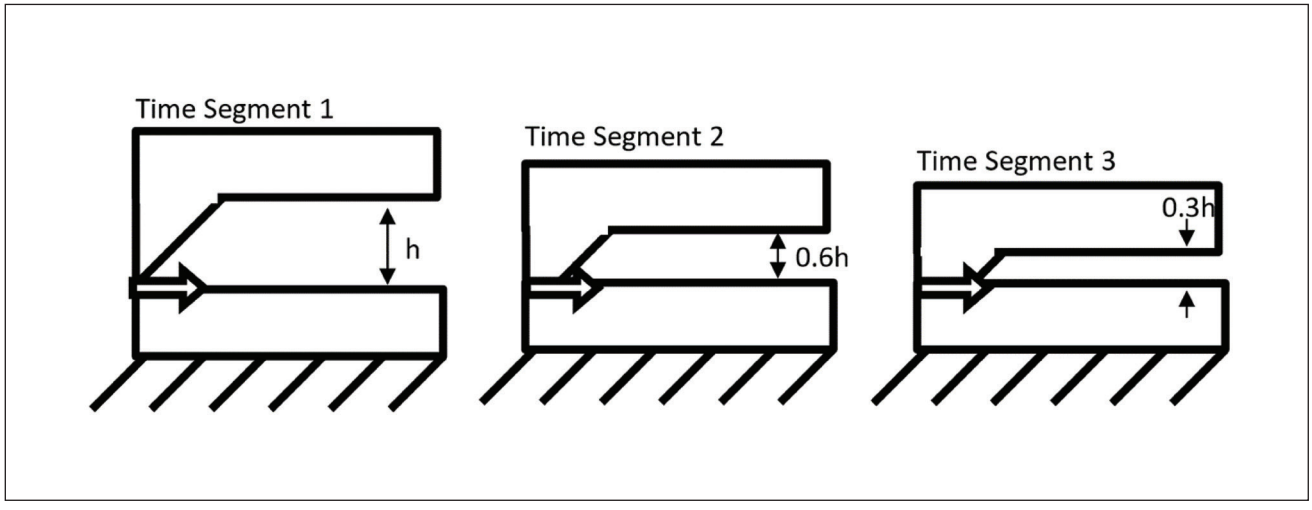

Fig. 5 — Diagram of approach to flow modeling, split along line of symmetry.

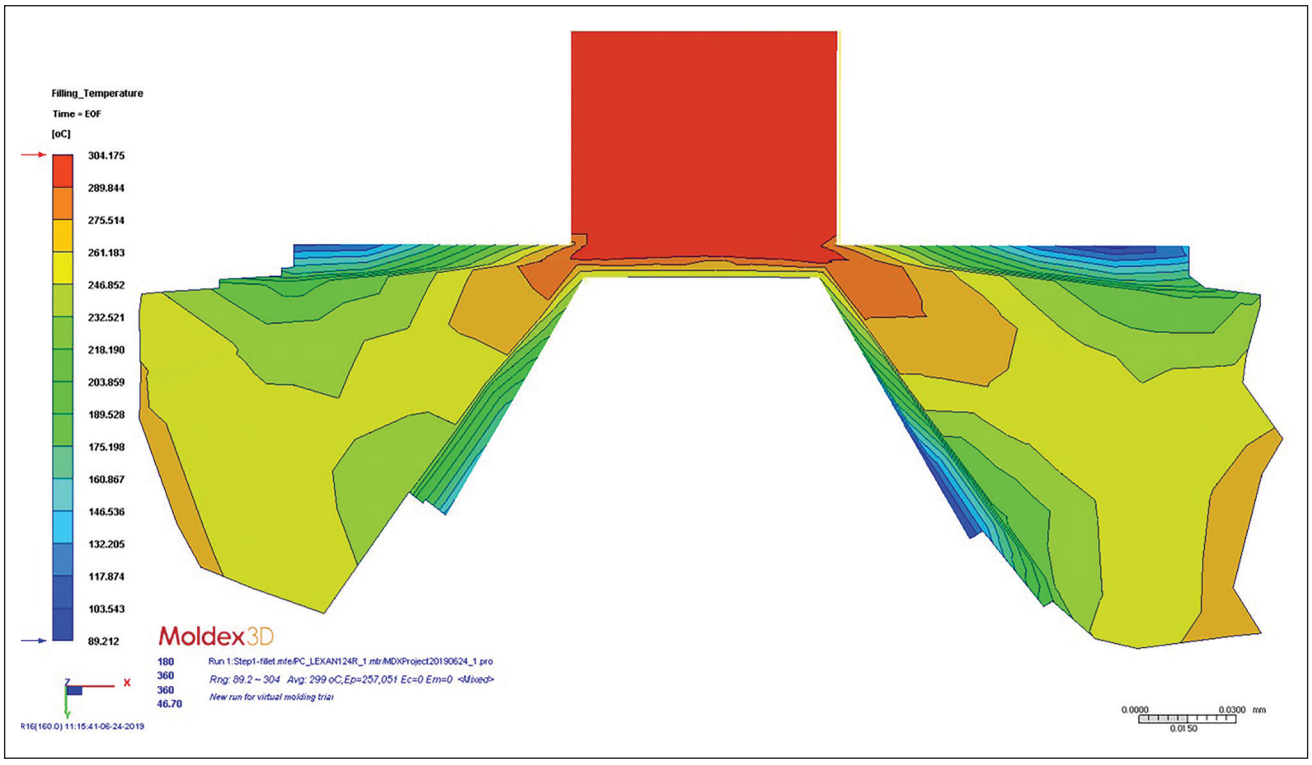

Fig. 6 — Simulation result from 10% energy director collapse, showing melt temperature distribution.

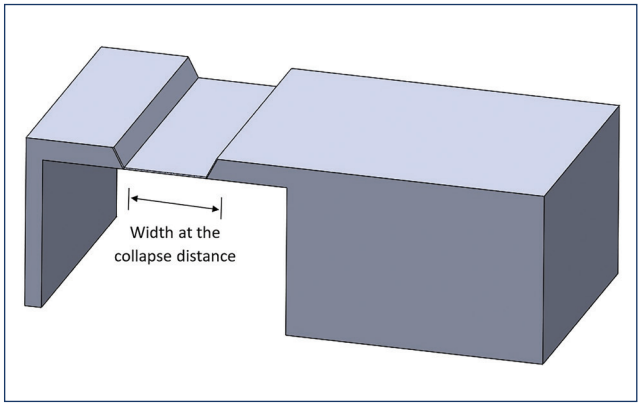

Fig. 7 — Model for simulation, representing the negative space between the two parts to be welded at the joint, for a collapse of 80% and a 60 deg energy director.

that show this effect and are in appropriate geometries are required to observe it (Ref. 39). In this work, the chain orientation of the welded samples was not measured due to the unsuitable part geometry.

Crystallinity

The crystallinity of the polymer weld will depend on the cooling rate and the shear stresses in the melt that are present when solidification begins (Refs. 40–47). Both factors affect how well or not the polymer chains will organize as they solidify. Several studies have investigated the effect of welding on the crystallinity of the polymer, but few have attempted to quantify or predict the change (Refs. 48, 49).

A study of microstructure in a laser weld by Abed et al. identified three distinct microstructure zones. The center zone of the weld, where the greatest heat was concentrated, was identified as Zone 1. Here, spherulites (regions of crystalline growth) were quite large compared to the bulk material. This is a result of the complete melting of the initial spherulites, which meant that nucleation was required before forming new spherulites during cooling. Since few of these formed, the spherulites could grow rather large (Ref. 48).

Zone 2 is just outside Zone 1, and Zone 3 is between Zone 2 and the bulk material. Zone 2 was defined by slightly smaller spherulites than Zone 1, which would be due to the incomplete melting of initial spherulites, allowing more nucleation sites to form. In Zone 3, minimal melting of the initial spherulite structure occurs, resulting in spherulites nearly the same size as the bulk. The increased spherulite size in the joint decreases elongation at break and yield stress in this area (Ref. 48).

Chung and Kamal found that increasing force during vibration welding results in the formation of smaller spherulites. This is because higher temperatures are reached with lower welding forces. The heat-affected zone is larger at lower temperatures, allowing a slower cooling rate and slower cooling rates to result in larger spherulites. Increased stress also results in greater nucleation, which could explain the smaller spherulite size (Ref. 50).

In general, greater crystallinity leads to greater tensile strength and reduced ductility. The crystalline growth type will depend on the material type and will not be a factor for amorphous polymers (Refs. 51, 52).

Table 1 — Simulation Inputs

	Weld Parameters			Simulation Inputs			
	Frequency (kHz)	Collapse (mm)	Trigger Force (N)	Max Pressure (MPa)	Filling Time (s)	Melt Temp (°C)	Fill (%)
ABS	20	0.38	315	44.8	0.379	230	3.57%
ABS	20	0.25	315	40.5	0.294	230	1.61%
ABS	20	0.38	463	67.3	0.143	230	3.57%
ABS	20	0.38	391	58.4	0.213	230	3.57%
ABS	30	0.38	233	15.8	0.791	280	3.57%
PC	20	0.38	374	76.9	0.925	350	2.00%
PC	20	0.25	374	69.3	0.674	350	0.87%
PC	20	0.38	496	94.3	0.645	350	2.00%
PC	20	0.38	636	111.3	0.475	350	2.00%
PC	30	0.38	435	35.4	0.653	350	2.00%
PBT	20	0.38	1232	167.0	0.345	305	2.00%
PBT	20	0.25	1232	165.4	0.317	305	0.87%
PBT	20	0.38	909	125.3	0.662	305	2.00%
PBT	20	0.38	632	96.5	1.164	305	2.00%
PBT	30	0.38	634	83.2	1.132	305	2.00%

The Avrami equation can predict the crystallization rate for spherulite growth (Ref. 53):

$$\phi_C = 1 - e^{-K(t)^m} \quad (9)$$

where ϕ_C is the crystallized fraction, K(t) is the rate constant, and m is the Avrami exponent. For three-dimensional crystal growth, m=3 and

$$K = \frac{4}{3}\pi N \dot{r}^3 \quad (10)$$

where N is the number of nuclei per unit volume at t=0, and $\dot{r}$ is the radial growth rate of the crystalline spheres [Ref. 53]:

The Avrami equation is valid only for fast cooling rates (> 60°C/min), as in the case of ultrasonic welding, due to localized melting. Another consideration is that the Avrami equation is most accurate, up to 50% crystallinity (Ref. 54). However, most crystallinity is less than 50% for polymers, so this should not be a barrier to practical use (Ref. 55). However, the Avrami variables need to be determined experimentally for each material.

Simulation Approach

It is proposed that the flow from the energy director can be modeled as flow from a set of gates forcing out melt in opposite directions using a common injection molding simulation package (such as MoldEx3D), similar to the diagram shown in Fig. 4.

Although the energy director is collapsing, the geometry of the weld joint remains the same throughout, as diagrammed in Fig. 5.

Figure 6 shows the initial segment weld collapse simulation when about 10% of the energy director melted; the part model for this simulation is shown in Fig. 7.

While the energy director is expected to melt in discrete segments, only the last step of the weld will be simulated. Even if the simulation were broken into distinct segments, the temperature and viscosity history of the melt and the

volume of melt already extruded could not be submitted to the simulation for the next step. The final expulsion of polymer melt before the end of the weld will dictate the velocity and viscosity of the plastic immediately before cooling. As such, these final estimates will be the most applicable to determining intermolecular diffusion, crystallinity, and orientation. The part will be modeled so that each side of the energy director is treated as a gate through which half of the melt will flow.

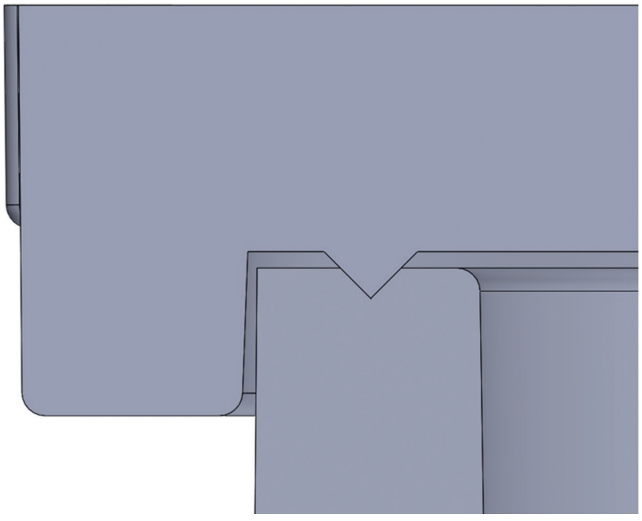

Fig. 8 — Assembly model, cross section of the joint (90 deg energy director).

The melt flow simulation was used to model all the flow expected in a single step at the target collapse distance. For example, if a collapse distance of roughly 80% of the energy director is programmed, the correlating volume of melt it would generate can be input to the model. For this purpose, a CAD model of the part geometry has been made. This geometry is the negative space between the two halves of the assembly and can be adjusted for energy director angle and collapse distance, as shown in Fig. 7.

This geometry can be compared to the model of the assembly when adjusted to the same gap, as shown in Fig. 8. This shows a cross-section of the assembly that will be welded, where a triangular energy director is on one part. The negative space between the two weld halves is then turned into the part model for the simulation (shown in Fig. 7).

The model to be used for the flow analysis continues beyond the flat to flat and into the flash trap on both sides. For this work, a short section of the weld joint was modeled as a straight section. It is assumed that the length of the energy director exceeds its width sufficiently to be considered infinite length, as would be the case for this circular energy director. Further, it is assumed that the circle's radius is so large compared to the energy director size that it can be safely considered straight for this model. In this simulation, only the flow at the center of the modeled straight section is of interest and estimated to be the same as what a typical cross-section would look on the larger part.

For plastic welders that apply a constant force, it is proposed that the final weld segment can be simulated under a constant force rather than a constant velocity. A constant

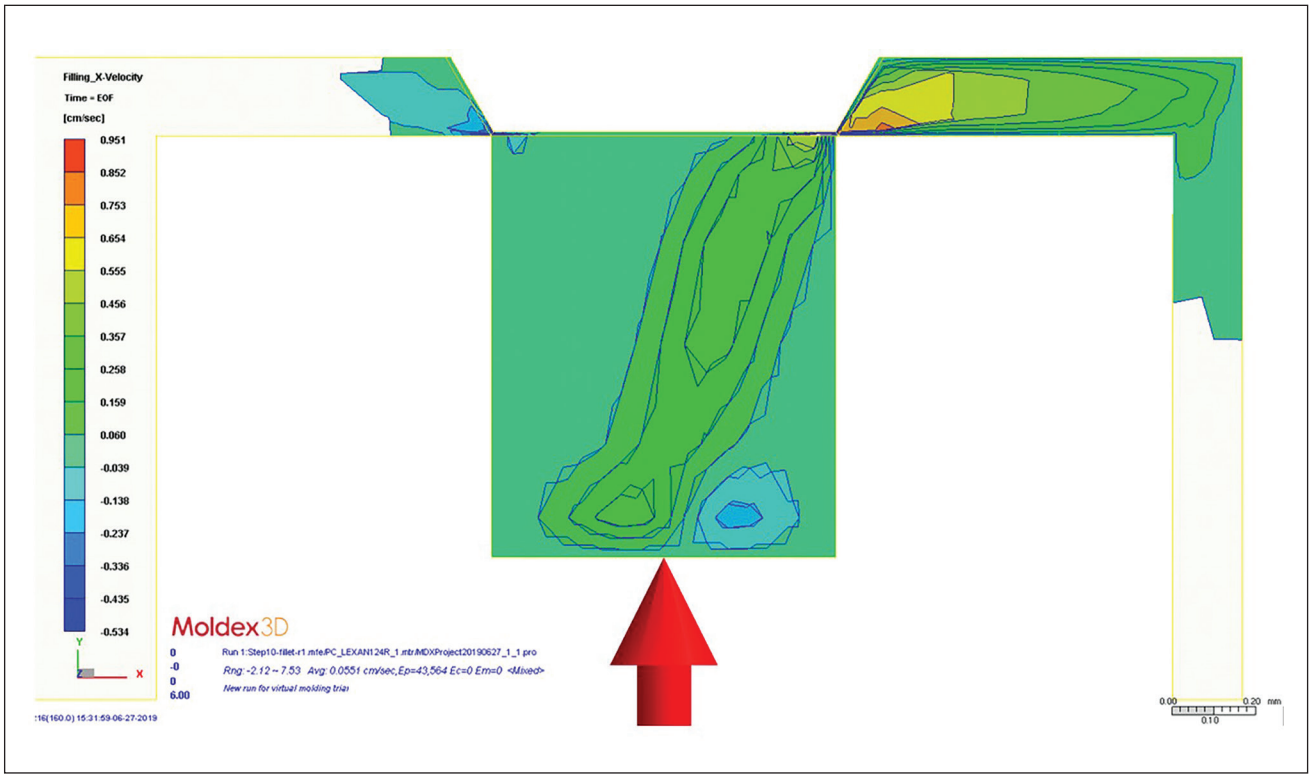

Fig. 9 — Placing a hot runner on only one side of a thicker section of the energy director leads to uneven flow that is not representative of reality.

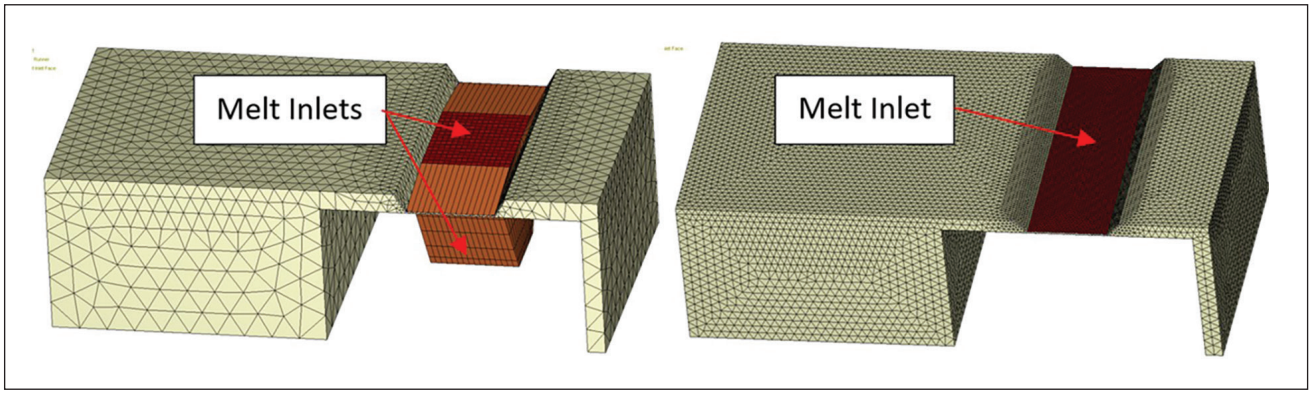

Fig. 10 — Comparison of melt inlet from the first simulation, left, and the final simulation, right.

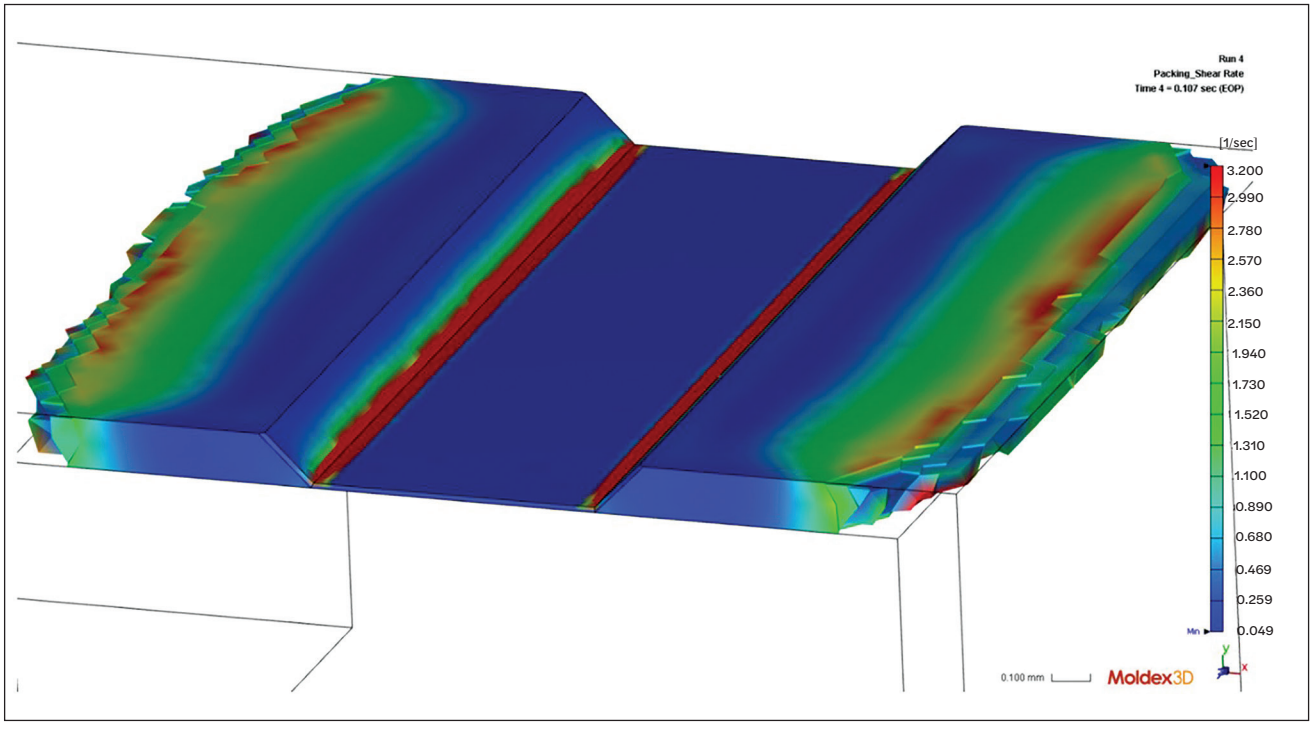

Fig. 11 — Shear rate of melt for an ABS joint.

force approach will yield the same key melt properties for integration into the final prediction of weld strength. The goal of the simulation portion of the model is to provide a plot of the velocity, viscosity, and temperature of the melt as a function of distance from the middle of the energy director to the edge of the melt flow zone.

Inputs

The key inputs needed to perform the simulation are melt temperature, mold temperature, maximum injection pressure, filling time, and percent of volume to inject. These parameters can be calculated or estimated based on the part geometry, material properties, and process parameters. The simulation will be limited by the time or injection volume, at which point the calculations cease.

In the simulation, the temperature of the hot runner is set to be the polymer's critical flow temperature, and the surrounding mold's temperature is set to room temperature. The maximum injection pressure is set according to the expected applied force divided by the cross-sectional area of the energy director at the set collapse distance. The time is set to the weld time setting during welding. The fill percent is the volume of energy director displaced at the set collapse distance divided by the model's total volume.

Table 1 shows the simulation inputs for the acrylonitrile butadiene styrene (ABS), polycarbonate (PC), and polybutylene terephthalate (PBT) models and the critical part dimensions needed to calculate them. For all runs, the mold and air temperature were set to 25°C, the packing time was set to 0.1 s, and the cooling time was set to 0.5 s. The packing

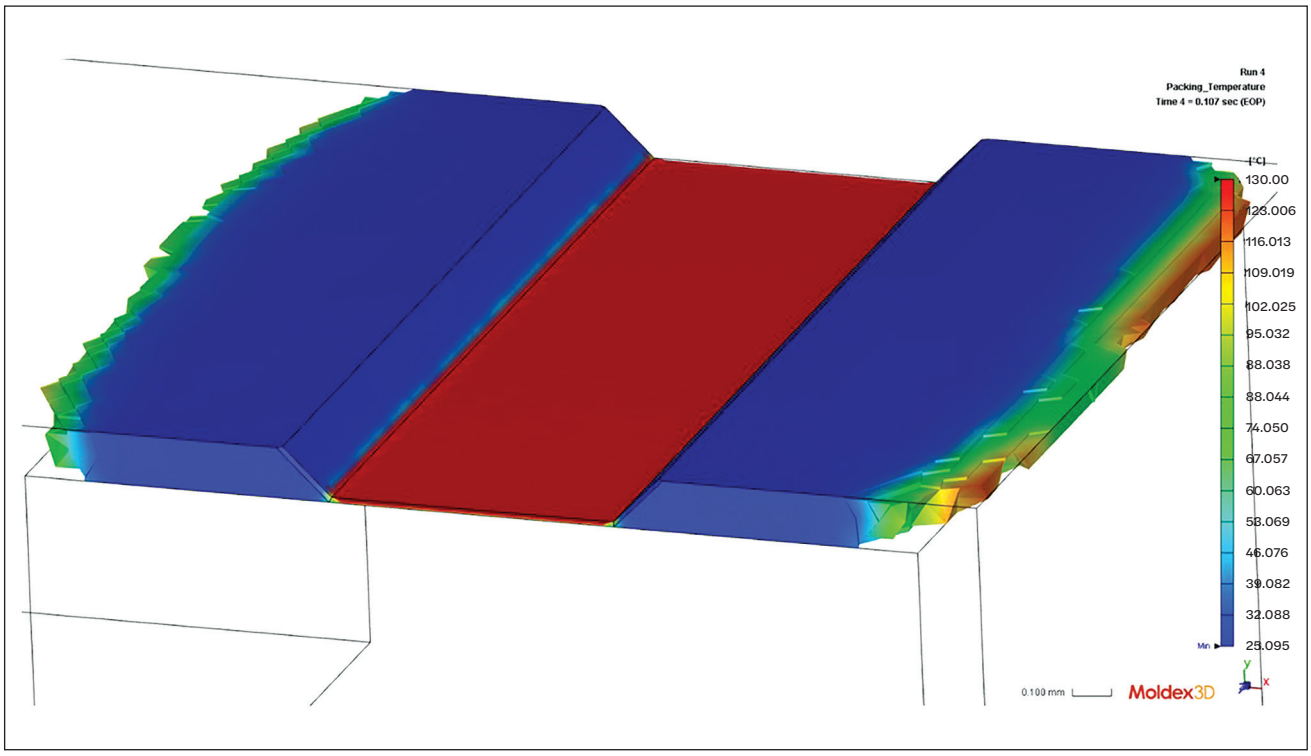

Fig. 12 — Melt front temperature for an ABS joint.

Table 2 — Material Data for Mold Properties

Property	Units	ABS	PBT	PC
Density	g/cm^3	1.026	1.288	1.16
Elastic Modulus	dyne/cm^2	2.57E+10	2.34E+10	2.34E+10
Poisson Ratio		0.4	0.38	0.4
Coefficient of Linear Thermal Expansion	1/K	8.63E-05	8.10E-05	6.84E-05

time is similar to the dynamic hold time, and the cooling time is similar to the static hold time during welding.

The critical flow temperature is generally considered 100°C above the glass transition temperature for amorphous plastics and about 15°C above the melting temperature for semi-crystalline plastics. Without this information, the temperature at which the melt flow index is measured can be used. The key is that the critical flow temperature is when the material acts more like a liquid than a solid.

The force being applied can be calculated as the maximum load before excessive deformation occurs or is established from known process parameters. Excessive deformation can be 1-5% of the energy director's height. The ambient temperature (room temperature) is set as the initial temperature of the mold, where the mold is simply the flash trap of the assembly being welded.

The mold properties were changed from the standard metal, as would be the case for an injection molded part, to polymer properties that match the material being welded to account for heat conduction into the bulk of the part. However, the simulation does not model the effect of this heating on the mold. The properties used are listed in Table 2 and were obtained from MoldEx 3D's material database. The heat capacity and thermal conductivity were input as tables to allow for temperature-dependent properties.

Outputs

For the simulation, the top and bottom of the energy director are set as hot runners with melt flow inlets on each side. At a very small collapse with a very thin energy director width, reasonable results could be achieved with a hot runner on only one side, as shown in Fig. 8. However, as the energy

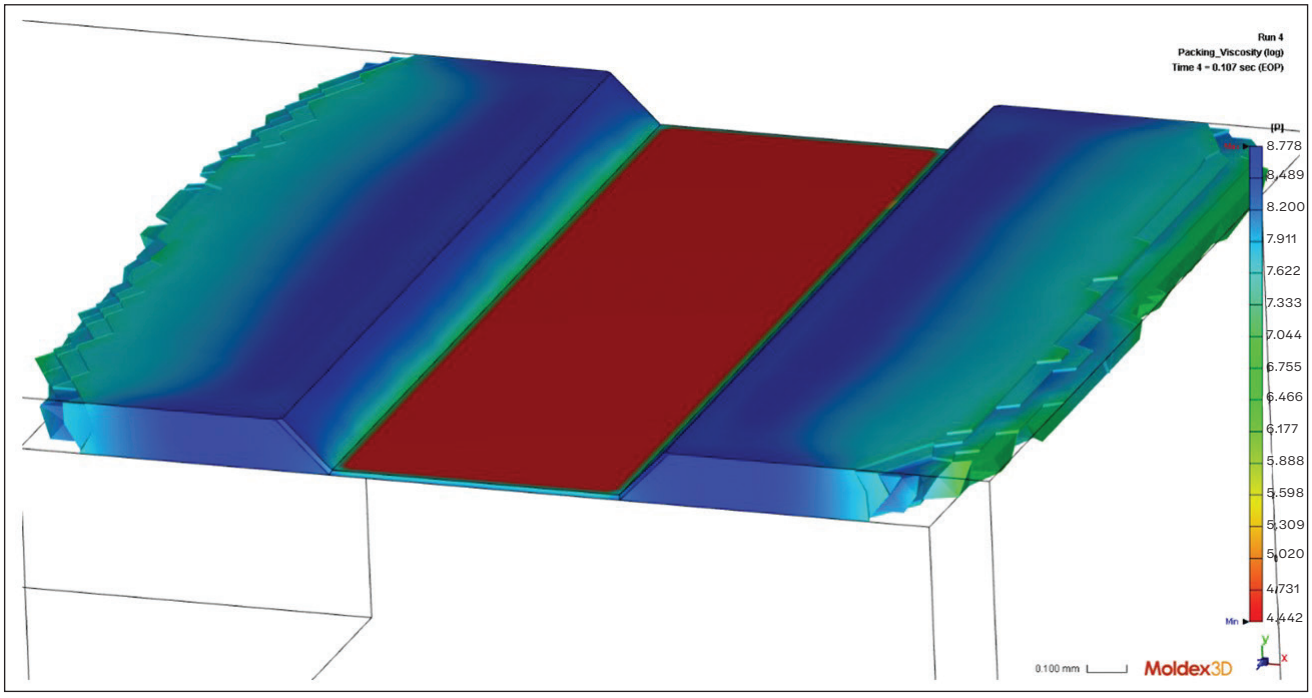

Fig. 13 — Viscosity of melt for an ABS joint.

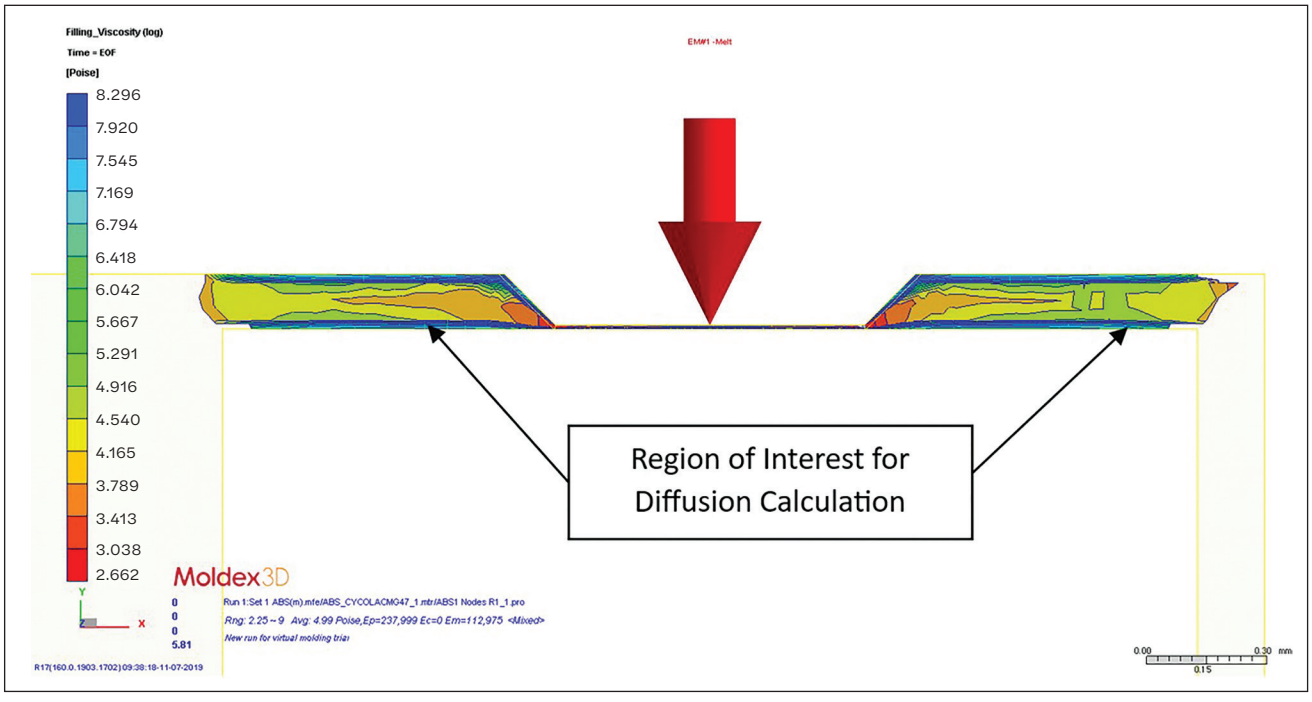

Fig. 14 — Viscosity model, ABS, 20 kHz, 0.38-mm collapse, 315 N trigger force, 0.03-mm amplitude.

director widens, the heat sink requirements for maintaining the opposite surface at the initial temperature become more pronounced, not reflecting reality as can be seen in Fig. 9.

During welding, the heat required for melting will quickly heat the surrounding material in intimate contact. Further, this heat will not dissipate because the polymer is highly insulated thermally. Therefore, it can be assumed that the temperature at the joint is the same on both sides of the collapsing energy director.

The elimination makes further improvements to the simulation process of the large gate. Using a large well of polymer melt as the inlet (Fig. 10, left) decreases the accuracy of the simulation by changing the boundary conditions as the polymer flows into the joint. In the new approach, the flat surface

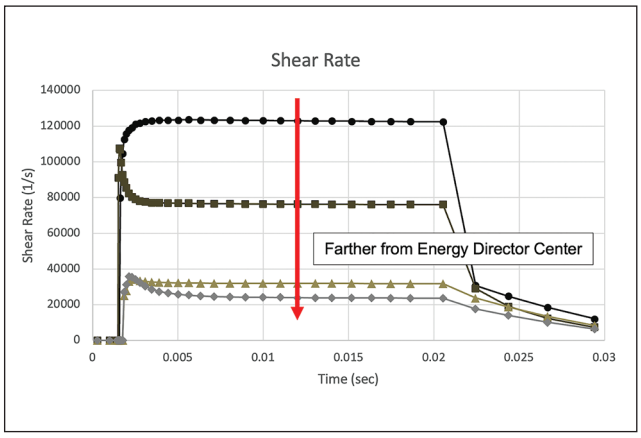

Fig. 15 — Shear rate at increasing distances from the energy director center vs. time, ABS, 20 kHz, 0.38-mm collapse, 315 N trigger force, 0.03-mm amplitude.

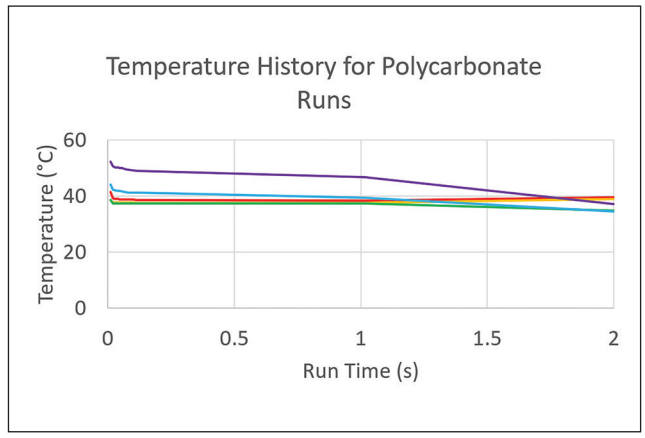

Fig. 16 — Temperature history for polycarbonate (data was collected at different locations, shown as different colors).

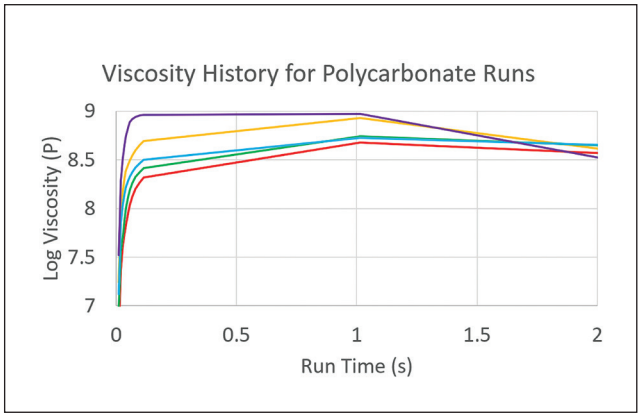

Fig. 17 — Viscosity history for polycarbonate (data was collected at different locations, shown as different colors).

of the collapsed energy director itself is selected as the melt inlet. Figure 10 shows the difference in the melt inlet from the first to the final simulation approach.

A reasonable model of the flow during welding can be achieved using the simulation inputs and the CAD geometry. Figures 11–13 show the shear rate, temperature, and viscosity results for a simulation of an ABS weld. This simulation was run in accordance with the parameters established in Table 1.

The data from the simulation can be incorporated into the equations proposed to account for the effects of various weld aspects on the weld strength. Per Equation 4, the viscosity in the middle of the flow region will be used to calculate the predicted diffusion, as marked in Fig. 14, which shows the viscosity in the melt region. It will be assumed that the energy director and bottom part material melt at a similar rate at the joint, and this weld material is pushed out of the weld zone together. As diffusion occurs fastest where the viscosity is lowest, the low-viscosity region in the middle of the flow zone will be selected and used to predict weld diffusion.

The shear rate history, shown in Fig. 15, can be used with Equation 8 to predict polymer chain orientation.

If the steady shear rate for each location is averaged, the rate is 63,795 s-1. Incorporating this and the flow time of 0.38 s (the weld time), the change in orientation trajectory is about 18.76 deg. This estimation is reasonable for the short time the polymer melt is under load before cooling. Any change in polymer orientation in the weld joint weakens the tensile strength as the direction of flow in the joint is parallel to the joint surface and, thus, perpendicular to the direction of tensile pull force.

A limitation of the simulation is that the temperature rise in the base material of the parts cannot be modeled. The energy director and surrounding joint geometry are considered an injection mold. The polymer material properties can be applied to the "injection mold" to ensure accurate modeling of the conduction loss to the surrounding part. However, the heat accumulated in the parts cannot be modeled using the existing software. When welding a joint with an energy director, however, most of the deformation occurs in the energy director, so the approximation of no change in the shape of the bulk material is considered acceptable for this case.

Simulation vs. Experimental Results

Intermolecular Diffusion

The viscosity and temperature data for the region were exported, as shown in Figs. 16 and 17 for the polycarbonate runs and used in conjunction with Equation 4 to find the expected degree of healing. The data was taken at multiple locations in the melt zone, indicated by different colors on the graphs, and then averaged.

The calculation for the degree of healing for a sample ABS run based on these same temperature and viscosity history data is shown in Table 3.

The equation results in a degree of healing greater than one, meaning there has been more than enough time for the polymer chain to diffuse entirely out of its initial tube. However, any "degree of healing" greater than one provides the

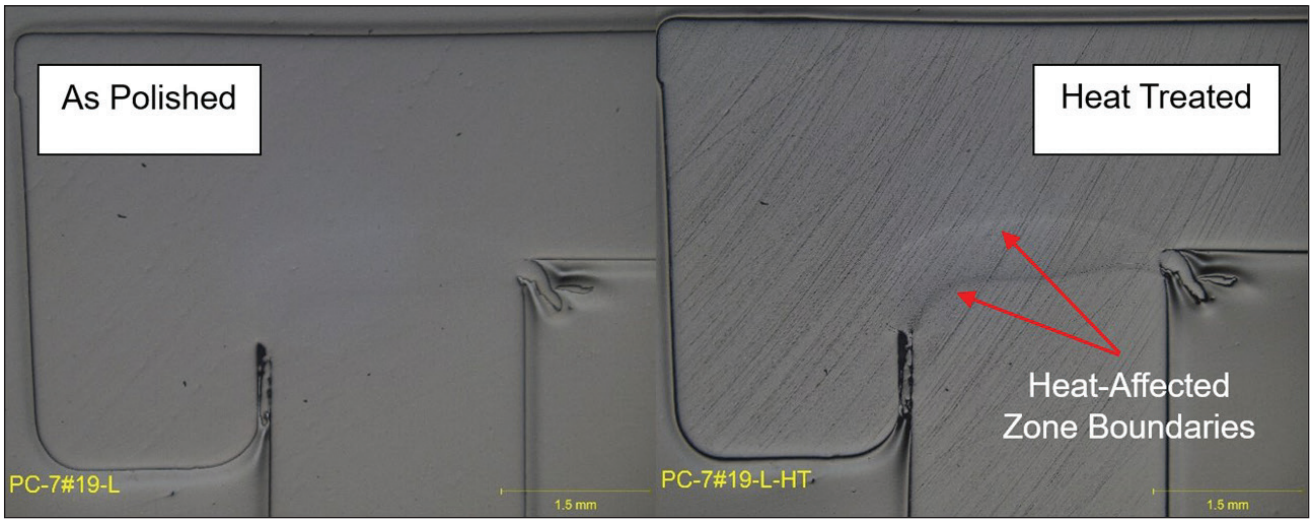

Fig. 18 — Cross section of PC weld showing good intermolecular diffusion.

Table 3 — Calculation of Degree of Healing with ABS

Equation Parameter	Units	Value
Average Integral of Temperature / Viscosity	$K*m*s^2/kg$	0.01330
Boltzman's Constant	$(m^2*kg)/(s^2*K)$	1.38065E-23
Avogadro Number	1/mol	6.02214E+23
ABS Density	kg/m^3	1026.0
ABS Monomer Molecular Weight	kg/mol	0.2113
Degree of Healing		3.48302

same strength benefit as a degree of healing of one. Therefore, this value essentially maxes out at one. For all simulated welds, the degree of healing was greater than one, which correlates well with observed cross-sectional results indicating that diffusion occurred in all the welds. However, the PBT welds appeared to experience separation after welding due to shrinkage during cooling.

When a polished cross-section of the joint is heat treated by applying hot air or infrared radiation to the surface, the polymer chains on the top surface — which have been mechanically smeared during polishing — experience thermal recovery, and a distinct line appears where there has been a change in the microstructure of the part (Ref. 28). When a weld has good intermolecular diffusion, as in Fig. 18, the heat-affected zone's boundaries appear, but there is no boundary line through the middle of the weld. When there is no diffusion, as in Fig. 19, a distinct line of separation can be seen at the interface.

Crystallinity

Dynamic scanning calorimetry (DSC) was used to measure the crystallinity of the semi-crystalline polymer (PBT) welds. A small amount of polymer was cut from the weld area and tested using the same DSC settings used to test the base material. The DSC data can be plotted versus time to calculate the melting and cold crystallization peak volume. Figure 20 shows the DSC plot, at a rate of 10°C/min, for one of the PBT welds with labeled cold crystallization and melting peaks.

The crystallinity of the sample, or volume transformed (V_T), can be calculated using Equation 11:

$$V_T = \frac{H_m - H_c}{H_0} \quad (11)$$

where H_m is the heat of fusion of melting, H_c is the heat of fusion of cold crystallization, and H_0 is the heat of melting of a 100% crystalline sample, which is 53 J/g for PBT (Ref. 56).

The heat of fusion of the melting and cold crystallization is found by the volume of each peak. The difference between

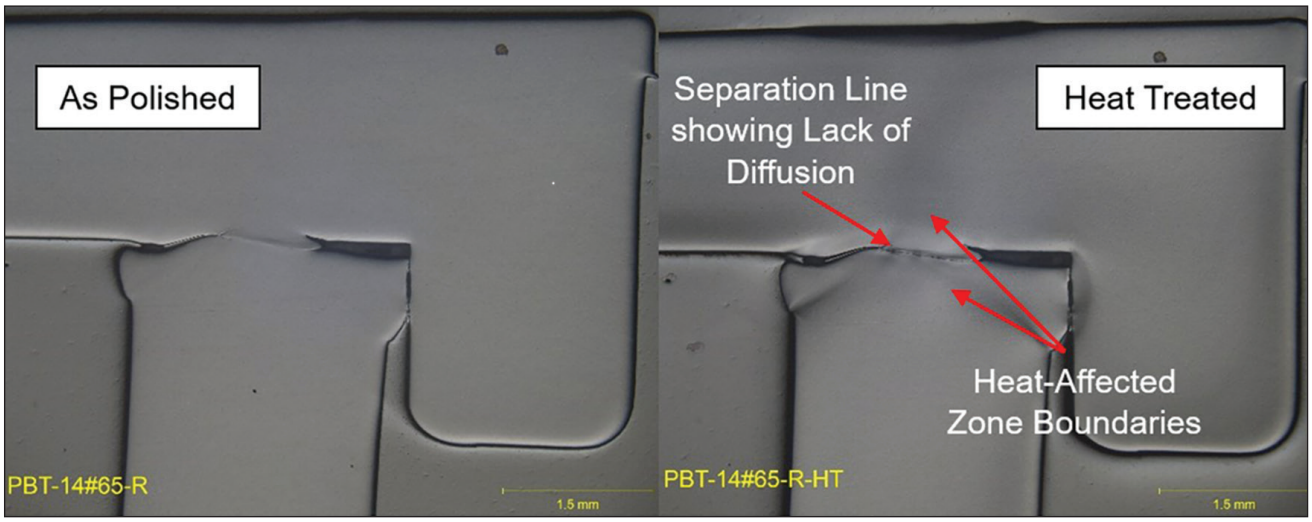

Fig. 19 — Cross section of PBT weld showing no intermolecular diffusion.

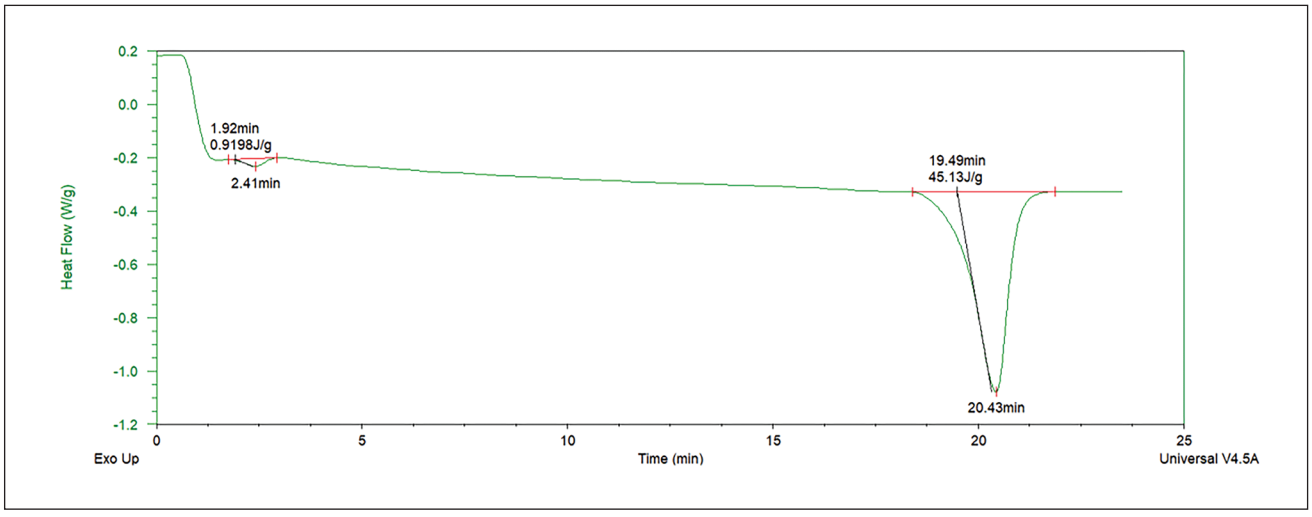

Fig. 20 — DSC data and analysis for PBT.

Table 4 — Crystallinity of the PBT Base Material

Sample	Hc (J/g)	Hm (J/g)	Crystallinity (Total %)
Cup 1	1.053	45.9	85%
Cup 2	1.484	46.86	86%
Lid 1	0.4095	47.64	89%
Lid 2	1.384	51.76	95%

these can be divided by the volume of the melting peak for a fully crystalline sample to see the crystallinity of the measured sample. The heat of fusion of melting for a fully crystalline material can be found in a reference table.

Using Equation 11, the base material's percent crystallinity was calculated and tabulated in Table 4. The average crystallinity of the base material is 89%.

The measured weld crystallinity as a percentage of the base crystallinity is listed in Table 5.

Table 5 — Crystallinity of the Weld for PBT Samples

	Frequency (kHz)	Collapse (mm)	Force (N)	Amp (mm)	Hc (J/g)	Hm (J/g)	Weld Crystallinity (Total %)	Weld Crystallinity
Constant Speed	20	0.38	1232	0.03	0	46.73	88%	99.5%
	20	0.25	1232	0.03	0.719	47.34	88%	99.3%
	20	0.38	909	0.025	0.649	48.68	91%	102.3%
	20	0.38	632	0.02	0.441	36.79	69%	77.4%
	30	0.38	634	0.02	0.677	47.4	88%	99.5%
Profiled Speed	20	0.38	1232	0.03	0.690	48.29	90%	101.4%
	20	0.25	1232	0.03	0.649	44.63	83%	93.7%
	20	0.38	909	0.025	0.920	45.13	83%	94.1%
	20	0.38	632	0.02	0.613	44.09	82%	92.6%
	30	0.38	634	0.02	0.864	46.01	85%	96.1%

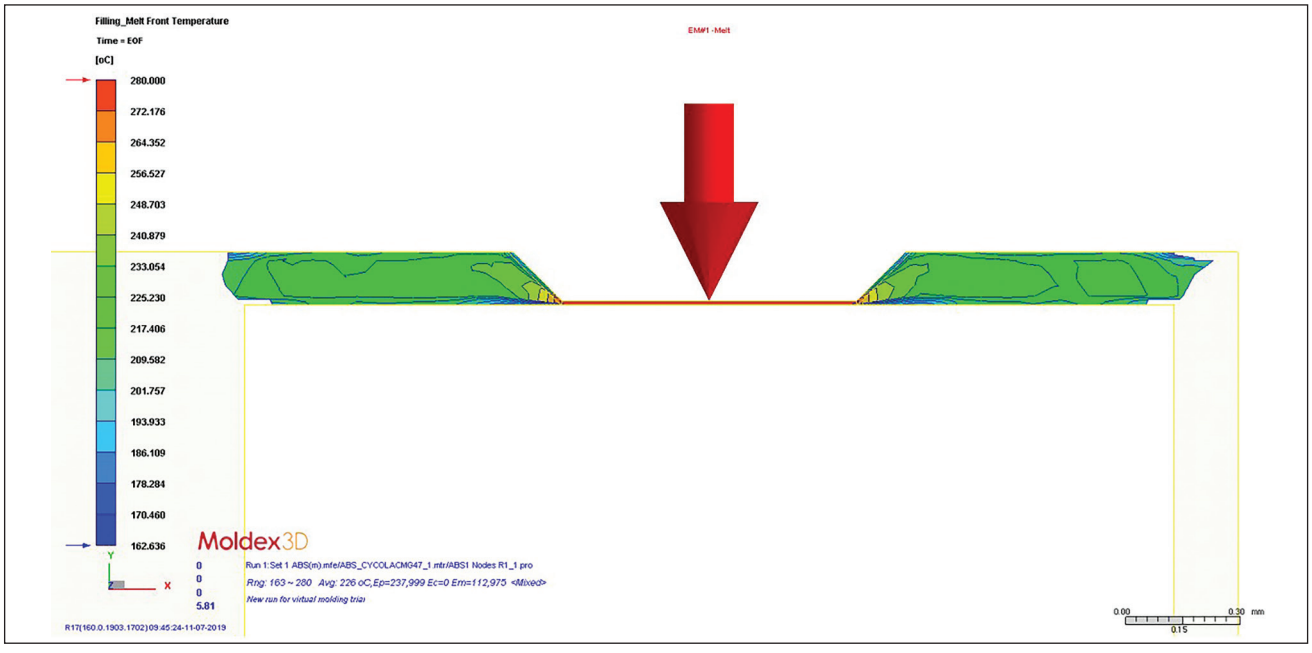

Fig. 21 — Melt front temperature model, ABS, 20 kHz, 0.38-mm collapse, 315 N trigger force, 0.03-mm amplitude.

The expected crystallinity was also an output from the simulation. Zhao et al. found that the crystallinity prediction from MoldEx 3D closely matched measured results (Ref. 57). However, the crystallinity predictions from the simulated welds in this work were much lower than the measured results. The simulations predicted nearly zero crystallinity at the end of the cooling phase for all cases, an unreasonable result. This unreasonable result may be due to the inability to account for the heat accumulated in the base material. Thus, the cooling rate in the model is expected to be significantly faster than the cooling rate in reality, making the predicted crystallinity much lower.

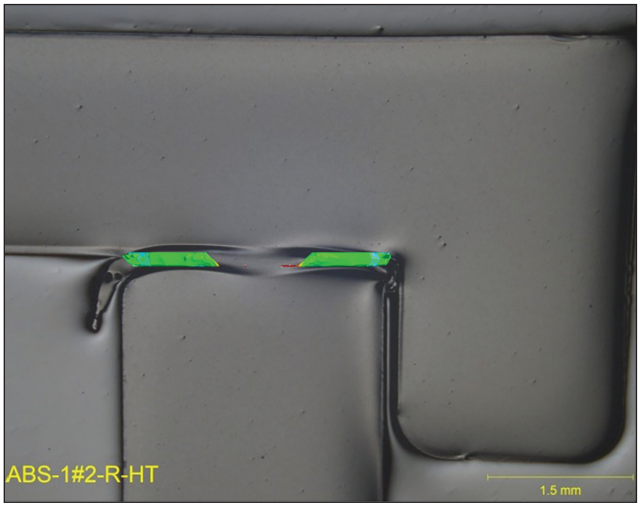

Fig. 22 — Cross section of welded ABS part with model flow overlaid.

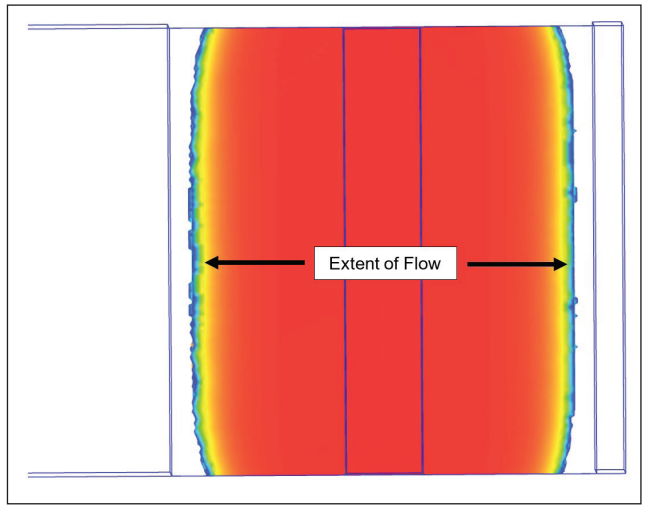

Fig. 23 — Simulation image showing notch length "a."

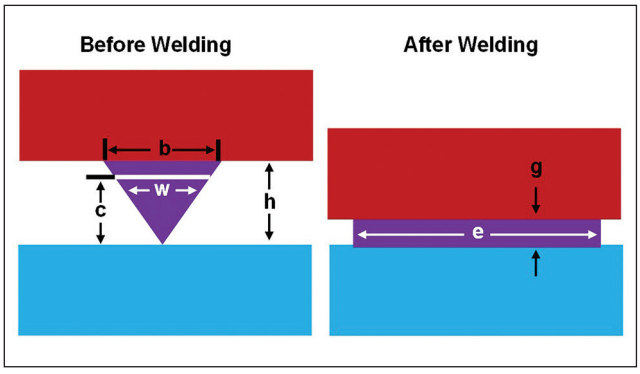

Fig. 24 — Joint geometry before and after welding.

Extent of Flow

The extent to which the melt flows is useful to determine the likelihood of polymer melt extruding from the weld joint (weld flash). Depending on the product being welded, this can be a cosmetic or functional issue. Functionally, weld flash may cause problems with fit-up, contamination, or stress concentration that can weaken the weld. Therefore, predicting the extent of melt flow during welding is quite useful.

The simulated extent of flow from the model is shown in Fig. 21. This is overlaid with a cross-section of a part welded at the simulated settings in Fig. 22.

The model's accuracy in predicting the extent of melt flow versus the experimental results was evaluated. Table 6 shows the measured welded width of parts welded at the same settings that were simulated.

The extent of flow was measured in MoldEx 3D to compare these results, as shown in Fig. 23.

A simple mathematical approach to finding the weld width was also evaluated by calculating the nominal volume of displaced material (V_D) and setting that equal to the volume available in the weld joint after the weld collapse, as illustrated in Fig. 24.

The relationship of the displaced energy director volume to the volume available for that melted material to fill after welding is defined in Equation 12:

$$V_D = [0.5bh - 0.5w(h - c)]L = geL \tag{12}$$

where b is the width of the energy director, h is the energy director height, w is the width of the triangle at the collapse distance, c is the collapse distance, L is the energy director length, g is the remaining joint gap, and e is the extent of flow.

The width of the energy director at the collapse distance, w, can be calculated by:

$$w = 2c\sin(\theta/2) \tag{13}$$

where θ is the angle of the energy director.

Combining and simplifying Equations 12 and 13, the extent of flow can be found:

$$e = \frac{0.5[bh - 2c(h - c)\sin(\theta/2)]}{g} = \frac{\sin(\theta/2)\,[h^2 - c(h - c)]}{g} \tag{14}$$

The gap height is the final distance between the joint surfaces in the weld area. The gap height is the total energy director height (which sets the initial gap) minus the collapse distance. However, the final gap is generally a bit more than this nominal, likely due to some inconsistency in the linear encoder feedback of the welder. For these calculations, the final gap will be estimated by:

$$g = (h - c) + 0.5\text{mm} \tag{15}$$

The extent of flow values found via measurement of the weld cross-section, simulation, and calculation are graphed

Table 6 — Measured Weld Width for All Materials and Settings

Material	Frequency (kHz)	Collapse (mm)	Trigger Force (N)	Amplitude (mm)	Weld Width (mm)
ABS	20	0.38	315	0.03	2.64
	20	0.25	315	0.03	1.20
	20	0.38	463	0.05	1.69
	20	0.38	391	0.04	2.04
	30	0.38	233	0.02	2.55
PC	20	0.38	374	0.035	2.31
	PC	0.25	374	0.035	2.02
	20	0.38	496	0.04	2.53
	20	0.38	636	0.045	2.56
	30	0.38	435	0.035	2.51
PBT Constant Speed	20	0.38	1232	0.03	1.58
	20	0.25	1232	0.03	0.83
	20	0.38	909	0.025	1.47
	20	0.38	632	0.02	0.82
	30	0.38	634	0.02	1.00
PBT Profiled Speed	20	0.38	1232	0.03	1.00
	20	0.25	1232	0.03	1.39
	20	0.38	909	0.025	0.99
	20	0.38	632	0.02	0.79
	30	0.38	634	0.02	0.92

in Figs. 25, 26, and 27 for the five parameters set welded with each material: ABS, PC, and PBT.

The simulated and calculated values for the flow extent are close to those determined from the measured extent of flow. The simulated values are a closer fit to the measured values than the calculated values, especially for the parameter sets with a reduced collapse distance (the second point on each of the graphs), and they provide useful predictions for all three model materials.

The average difference between the measured and simulated values is 0.037 mm, while the average difference between the measured and calculated values is 0.465 mm. The average weld width of 1.93 mm means the simulation is accurate to about 2%, while the calculation method is only accurate to about 24%. In other words, the simulation offers a twelve times improvement in accuracy over the geometrical calculation.

Conclusions

As applications for plastics continue to become more complex and demanding, the weld requirements in these assemblies will also become stricter. Further, the total assembly cost will grow as specialized engineering polymers enclose expensive electronics or other costly internal components.

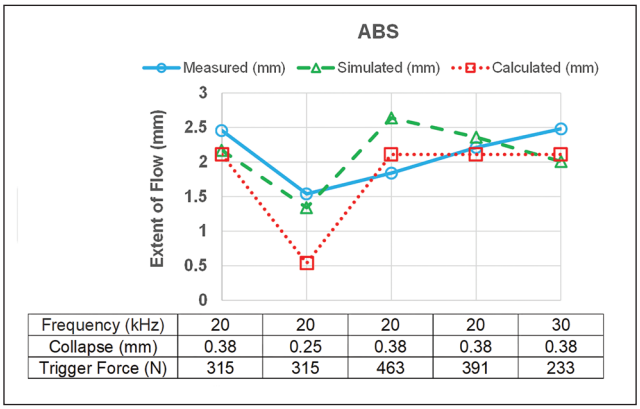

Frequency (kHz)	20	20	20	20	30
Collapse (mm)	0.38	0.25	0.38	0.38	0.38
Trigger Force (N)	315	315	463	391	233

Fig. 25 — Comparison of extent of flow for ABS.

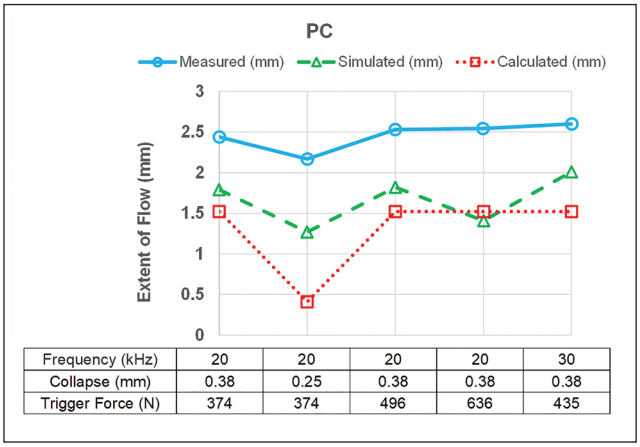

Frequency (kHz)	20	20	20	20	30
Collapse (mm)	0.38	0.25	0.38	0.38	0.38
Trigger Force (N)	374	374	496	636	435

Fig. 26 — Comparison of extent of flow for PC.

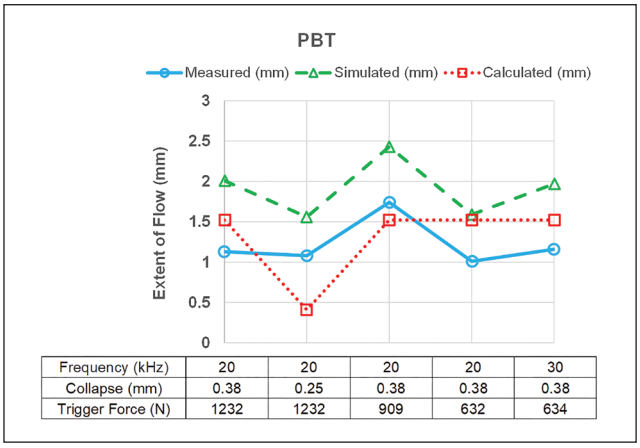

Frequency (kHz)	20	20	20	20	30
Collapse (mm)	0.38	0.25	0.38	0.38	0.38
Trigger Force (N)	1232	1232	909	632	634

Fig. 27 — Comparison of extent of flow for PBT.

The cost of process development via the traditional method of applying prior knowledge to find initial settings and then destructively testing hundreds or thousands of initial parts is growing. As this trend continues, the ability to model the welding process will become more important.

Modeling the welding process using commercial injection molding software provides a simple and relatively fast way to predict the extent of melt flow. Importantly, the extent of flow in the weld can be applied to determine whether flash should be expected. The joint design can then be optimized to contain a flash before the mold is machined. Additionally, the modeling approach provides reasonable data for calculating the expected degree of healing in the weld zone. However, this approach has not produced reasonable predictions of crystallinity in the weld material.

To improve the accuracy of the results, the modeling program would need to be able to apply motion during the simulation. The compression of the two welded surfaces is a key component of the process, the effects of which cannot currently be described by the model.

References

1. Morris, B., and Scherer, J. 2013. Preventing squeeze-out of sealant during hot bar sealing. *FlexPackCon*: 1452–1459.

2. Hartman, B. 1984. Temperature and pressure dependence of polymer melt viscosity. *Proceedings IX International Congress on Rheology*: 521–527.

3. Patham, B., and Foss, P. 2011. Thermoplastic vibration welding: Review of process. *Polymer Engineering Science* 51: 1–22.

4. Lyngaae-Jorgensen, J. 1984. Relationships between rheological functions in simple flows and measureable structural parameters for concentrated polymer melts. *Proceedings IX International Congress on Rheology*: 503–513.

5. Cao, W., Wang, T., Yan, Y., Qi, Y., Zhang, S., Li, Q., and Shen, C. 2015. Evaluation of typical rheological models fitting for polycarbonate squeeze flow. *Journal of Applied Polymer Science*: 132(29). DOI: 10.1002/app.42279

6. Starostin, N., and Ammosova, O. 2008. Heated tool flash welding of polyethylene pipes at low environment temperatures – Mathematical modelling of the thermal process. *Welding International* 22(1): 51–54.

7. Levy, A., Le Corre, S., and Villegas, I. 2014. Modeling of the heating phenomena in ultrasonic welding of thermoplastic composites with flat energy directors. *Journal of Materials Processing Technology* 214: 1361–1371.

8. Dodin, M. G. 1981. Welding mechanisms of plastics: A review. *The Journal of Adhesion* 12(2): 99–111.

9. McIlroy, C., and Olmsted, P. 2017. Disentanglement effects on welding behaviour of polymer melts. *Polymer* 123: 376–391.

10. Fourche, G. 1995. An overview of the basic aspects of polymer adhesion. Part I: Fundamentals. *Journal of Polymer Engineering and Science* 35(12): 957–967.

11. Sarabadani, J., Milchev, A., De Virgiliis, A., and Vilgis, T. 2014. Molecular dynamic study of the structure and dynamics of polymer melt at solid surfaces. *Soft Materials* 12(Sup1): S56–S70.

12. Wendel, H., and Noolandi, J. 1982. Generalized reptation model. *Macromolecules* 15: 1318–1320.

13. Edwards, S. 1967. The statistical mechanics of polymerized material. *Proceedings of the Physical Society* 92: 9.

14. Bousmina, M., Qiu, H., Grmela, M., and Klemberg-Sapieha, J. 1998. Diffusion at polymer/polymer interfaces probed by rheological tools. *Macromolecules* 31: 8273–8280.

15. Bastien, L., and Gillespie, J. 1991. A non-isothermal healing model for strength and toughness of fusion bonded joints of amorphous thermoplastics. *Journal of Polymer Engineering Science* 31: 1720–1730.

16. Yang, F., and Pitchumani, R. 2002. Healing of thermoplastic polymers at an interface under non-isothermal conditions. *Macromolecules* 35: 3213–3224.

17. Coogan, T., and Kazmer, D. 2017. Healing simulation for bond strength prediction of FDM. *Rapid Prototyping Journal* 23(3): 551–561.

18. Wool, R. 1984. Strength Development at a Symmetric Polymer-Polymer Interface. *Proceedings IX International Congress on Rheology*: 573–580.

19. Willett, J., O'Connor, K., and Wool, R. 1985. Mechanical properties of polymer-polymer welds: time and molecular weight dependence. *IACS Polymer. Preprints*: 26(2): 123–125.

20. Grewell, D., and Benatar, A. 2008. Semi-empirical, squeeze flow, and intermolecular diffusion model. ii. Model verification using laser microwelding. *Polymer Engineering and Science* 1543–1549.

21. McLeish, T. 2002. Tube theory of entangled polymer Dynamics. *Advances in Physics* 51(6): 1379–1527.

22. Watanabe, H. 1999. Viscoelasticity and dynamics of entangled polymers. *Progress in Polymer Science* 24: 1253–1403.

23. Ezekoye, O., Lowman, C., Fahey, M., and Hulme-Lowe, A. 1998. Polymer weld strength predictions using a thermal and polymer chain diffusion analysis. *Polymer Engineering and Science* 38(6): 976–991.

24. Doi, M., and Edwards, S. 1978. Dynamics of concentrated polymer systems part 1 - Brownian motion in the equilibrium state. *Journal of the Chemical Society* 12: 1789–1801.

25. Bueche, F. 1952. Viscosity, self-diffusion, and allied effects in solid polymers. *The Journal of Chemical Physics* 20(12): 1959–1964.

26. Guo, S., Ait-Kadi, A., and Bousmina, M. 2004. A modified model predictions and experimental results of weld-line. *Polymer* 45: 2911–2920.

27. Dealy, J., and Wissbrun, K. 1999. *Melt rheology and its role in plastics processing*.

28. Marcus, M. 2018. Methods of polymer weld quality evaluation. *ANTEC*.

29. Al-Wohoush, M., Sánchez-García, S., and Kamal, M. 2007. Microstructure of thermoplastic laser welded joints. *ANTEC*: 2803–2807.

30. Cai, L., Byrd, P., Zhang, H., Schlarman, K., Zhang, Y., Golub, M., and Jing, Z. 2016. Effect of printing orientation on strength of printed abs plastics. *The Minerals, Metals & Materials Society Annual Meeting*: 199–204.

31. Le, X., Akouri, R., Latassa, A., Passemato, B., and Wales, R. 2016. Mechanical Property testing and analysis of 3d printing objects. *Proceedings of the ASME 2016 International Mechanical Engineering Congress and Exposition*.

32. Vidakis, N., Vairis, A., Petousis, M., Savvakis, K., and Kechagia, J. 2016. Fused deposition modeling parts tensile strength characterisation. *Academic Journal of Manufacturing Engineering* 14(2): 87–94.

33. Krimm, S., Liang, C. Y., and Sutherland, G. 1956. Infrared spectra of high polymers. ii. Polyethylene. *The Journal of Chemical Physics* 25(3): 549–562.

34. Upadhyay, K., Dwivedi, R., and Singh, A. 2017. Determination and comparison of the anisotropic strengths of fused deposition modeling P400 ABS. *Advances in 3D Printing & Additive Manufacturing Technologies*: 9–28.

35. Uddin, M., Sidek, M., Faizal, M., Ghomashchi, R., and Pramanik, A. 2017. Evaluating mechanical properties and failure mechanisms of fused deposition modeling acrylonitrile butadiene styrene parts. *Journal of Manufacturing Science and Engineering* 139: 081018.

36. Rybachuk, M., Mauger, C., Fiedler, T., and Öchsner, A. 2017. Anisotropic mechanical properties of fused deposition modeled parts fabricated by using acrylonitrile butadiene styrene polymer. *Journal of Polymer Engineering* 37(7): 699–706.

37. Shieu, F., Wang, B., and Wu, J. 1997. Morphology and joint strength of polycarbonate-acrylonitrile/butadiene/styrene polymer blend. Plastics. *Rubbers and Composites Processing and Applications* 26(5): 230–234.

38. Macosko, C. 2003. *Rheology: principles, measurements, and applications*. Wiley.

39. Ling, X. On the fine structure of poly(L-lactic acid) filaments. Masters thesis, University of Tennessee, 48–51.

40. Strand, S., Sorenson, C., and Nelson, T. 2003. Effects of friction stir welding on polymer. *ANTEC*: 1078–1082.

41. Peggs, I. 1985. Fractography and metallography of polymers. *Microstructural Sciences* 12: 423–434.

42. Stevens, Abington. 1995. The effect of welding on the α- and β- crystalline forms of polypropylene. *ANTEC*: 1196–1200.

43. Oliveira, M., and Helmsley, D. 1985. The microstructure of polypropylene welds as a guide to processing history. *British Polymer Journal* 17(3): 269–274.

44. Bates, P., and Powell, A. 2009. Vibration welding polypropylene - Effect of MFI on weld strength and microstructure. *ANTEC*: 317–322.

45. Aris-Brosou, M., Vincent, M., Agassant, J., and Billon, N. 2017. Viscoelastic rheology in the melting and crystallization domain: Application to polypropylene copolymers. *Journal of Applied Polymer Science* 134: app.44690.

46. Lim, J., and Park, J. 2005. Weld-line characteristics of polycarbonate/acrylonitrile–butadiene–styrene blends. I. Effect of the processing temperature. *Journal of Applied Polymer Science* 95(3): 689–699.

47. Schlarb, A., and Ehrenstein, G. 1989. The impact strength of butt welded vibration welds related to microstructure and welding history. *Polymer Engineering and Science* 29(23): 1677–1682.

48. Abed, S., Laurens, P., Carretero, C., Deschamps, J., and Duval, C. 2003. Diode laser welding of polypropylene: Investigations of the microstructures in the welded seam. *Proceedings SPIE 4831, First International Symposium on High-Power Laser Macroprocessing* 4831: 77–81.

49. Nandhini, R., Kesava Moorthy, M., and Muthukumaran, S. 2017. Effect of welding parameters on microstructure. *International Polymer Processing XXXII* 4: 416–424.

50. Chung, Y., and Kamal, M. 2008. Morphology of pa-6 vibration welded joints and its effect on weld strength. *Polymer Engineering and Science* 48: 240–248.

51. Bartosiewicz, L., and Kelly, C. 1986. Microscopy techniques used in polymer research. *Advances in Polymer Technology* 6(2): 185–192.

52. Lebaut, E., Bates, P. J., and Kontopoulou, M. 2003. Effect of polypropylene rheology on the vibration welding process. *ANTEC*: 1068–1072.

53. Hiemenz, P., and Lodge, T. 2007. Crystalline polymers. *Polymer Chemistry*.

54. Müller, A., Michell, R., and Lorenzo, A. 2016. Isothermal crystallization kinetics of polymers. *Polymer Morphology*: 181–203.

55. Lotz, B. 1997. The structure and morphology of crystalline polymers. *Nuclear Instruments and Methods in Physics Research Section B*: 131: 13–21.

56. Wunderlich, B. 2005. *Thermal Analysis of Polymeric Materials*. Appendix 1: Table of thermal properties of linear macromolecules and related small molecules the ATHAS data banka.

57. Zhao, P., Wang, X., Fu, J., and Turng, L. 2016. Fast prediction of crystallinity in injection molding during packing phase. *ANTEC*: 182–186.

58. Grewell, D. 2005. Modeling of molecular healing for micro-laser welding of plastics with diffractive optical elements as spatial modulators. PhD thesis, The Ohio State University.

MIRANDA MARCUS (*mmarcus@ewi.org*) is with the Edison Welding Institute, Columbus, Ohio, and **EROL SANCAKTAR** is with the University of Akron, Akron, Ohio.